Acta Crystallographica Section A
Foundations of Crystallography
ISSN 0108-7673

Received 19 April 2005
Accepted 7 June 2005

Three-beam resonant X-ray diffraction in germanium – Laue transmission cases

Gunnar Thorkildsen,[a]* Helge B. Larsen,[b] Edgar Weckert,[c] Frode Mo[d] and Ragnvald H. Mathiesen[e]

[a]Department of Mathematics and Natural Science, University of Stavanger, N-4036 Stavanger, Norway, [b]Department of Materials Science, University of Stavanger, N-4036 Stavanger, Norway, [c]HASYLAB at DESY, Notkestrasse 85, D-22607 Hamburg, Germany, [d]Department of Physics, Norwegian University of Science and Technology, N-7491 Trondheim, Norway, and [e]SINTEF, Applied Physics Department, N-7465 Trondheim, Norway. Correspondence e-mail: gunnar.thorkildsen@uis.no

Perturbation of the two-beam diffracted power owing to the influence of a third lattice node has been examined for various three-beam cases in a small finite germanium crystal in the vicinity of the *K*-absorption edge. Although the crystal was slightly imperfect, the main parts of the experimental results are very well described within the framework of the fundamental theory of X-ray diffraction in conjunction with Cromer–Liberman calculations for the resonant scattering terms. Beam divergence and dynamical block size are treated as adjustable parameters in the analysis. Observed changes in the three-beam profile asymmetry are mainly attributed to size and not to resonance effects associated with the triplet phase sum of the involved reflections. Close to the absorption edge there is however some evidence indicating that f' values should be reduced in magnitude compared to the tabulated ones.

1. Introduction

In order to study the atomic and electronic structure of matter, the use of X-ray diffraction from systems in excited states or under resonance conditions is of significant importance (Coppens, 1992; Materlik *et al.*, 1994). For example, when the incident X-rays are tuned to an energy close to an electronic transition for one kind of the constituent atoms of the diffracting system, resonant processes (or, in this context, often called anomalous dispersion) take place. This effect gives a wavelength-dependent contribution to the scattering amplitudes and subsequently alters, both in phase and magnitude, the corresponding structure factors. In general, standard two-beam diffraction techniques have been applied to quantify and analyze this feature. However, as shown by Chang, Stetsko and co-workers (Chang, 1986; Stetsko, Lin *et al.*, 2001; Stetsko, Juretschke *et al.*, 2001), the use of three-beam diffraction as a complementary technique may prove interesting for such cases too. Here, a rotation (often called ψ rotation) is performed about a (primary) reciprocal-lattice vector, **h**, in order to gradually excite a third reciprocal-lattice node onto the Ewald sphere. The corresponding (secondary) reciprocal-lattice vector is denoted **g**. The resulting perturbations of the monitored two-beam intensity level may carry information about the triplet phase sum, Φ_Σ, of the involved reflections:

$$\Phi_\Sigma = \phi_{hg} + \phi_{go} - \phi_{ho}, \qquad (1)$$

where $\{\phi_{pq}\}$ represent the phases of the individual structure factors constituting the triplet. These are thus sensitive to any phase changes, $\phi_f(\lambda)$, invoked by the resonance conditions where the atomic form factor, f, becomes a complex quantity: $f \rightarrow f^0 + f'(\lambda) + if''(\lambda) = |f(\lambda)| \exp[i\phi_f(\lambda)]$. Here, f' and f'' denote the well known (isotropic) anomalous dispersion correction terms. λ is the X-ray wavelength. Hence, Φ_Σ may be a sensitive 'signature' of resonance effects (Larsen & Thorkildsen, 1998). However, a detailed analysis and interpretation (and possible parameter extraction) of the resulting profiles require discussion and thorough consideration of several other important quantities. 'Intrinsic' characteristics, like phase-insensitive contributions from *Umweganregung* and *Aufhellung*, have been extensively discussed in the literature; consult, for instance, Chang (1992) and Weckert & Hümmer (1997). Polarization-sensitive features have been the subject of detailed investigations too (Stetsko *et al.*, 2004). More practical issues with regard to identifying additional (interfering) reciprocal-lattice nodes in the immediate proximity of the Ewald sphere (Tanaka & Saito, 1975) and the rotation sense of the crystal were early highlighted (Chang, 1982; Hümmer & Billy, 1982). In addition to these properties, it is essential to consider crystal and diffraction geometry as well as crystal imperfections (Thorkildsen *et al.*, 2003). The latter is a challenge to treat – normally no additional information about the defect structure is known prior to a three-beam diffraction experiment, and very few worked-out 'real-crystal' theories are at hand (Larsen *et al.*, 2005). Geometry considerations, on

the contrary, are somewhat more straightforward to relate to. It has been shown that geometrical effects are of great importance especially for pure Laue–Laue transmission cases where the ratios between the effective crystal thickness and the appropriate extinction lengths are among the governing quantities in the interpretation of the resulting profiles (Thorkildsen & Larsen, 1998; Weckert & Hümmer, 1998). In this respect, it is important to realize that, since the extinction length is proportional to $(|F_{p-q}||F_{q-p}|)^{-1/2}$, F_{p-q} being the structure factor associated with the reflection $p-q$, it is sensitive to resonance-induced changes in f as well.

In the following, we present an experimental study at the K edge of germanium for a finite crystal. The scattering geometry for the three-beam cases explored is Laue transmission and the reflections involved have structure factors in the range 83–176 as calculated for $\lambda = 1.000$ Å. Thus they are all chosen among the ten strongest groups of reflections. As pointed out by Stetsko and co-workers (Stetsko, Lin *et al.*, 2001), these may not be the ideal cases for the study of resonant effects alone but are in general suitable for verifying different aspects of dynamical diffraction. Crystal geometry in particular turns out to be crucial for modeling the fine features of the collected ψ-scan profiles. The crystal under investigation was not ideally perfect, as revealed by two-beam rocking-curve measurements, but showed a small anisotropic broadening. In the accompanying simulations, this is modeled by treating the average dimension of the crystalline medium responsible for the coherent interactions, in the following called the dynamical block size, as a free parameter and performing a convolution in appropriate angular variables, here accounted for by the beam divergencies.

We begin this article with a brief review of the fundamental theory of n-beam X-ray diffraction. The basis for this can be found in the paper by Colella (1974). Here, however, we include a novel analysis for the excitation errors that is imperative for a proper modeling of the experimental results. The present treatment excludes any effects arising from the anisotropy of the scattering environment (Kokubun *et al.*, 1998, 2004; Lee *et al.*, 2001).

2. Theory

2.1. Fundamental equations

The displacement field within a crystal being exposed to incoming X-rays is expressed by the Ewald wave

$$\mathbf{D}(\mathbf{r}, t) = \sum_p \mathbf{D}_p \exp[2\pi i(\nu t - \mathbf{k}_p \cdot \mathbf{r})]. \quad (2)$$

The constituent waves build a self-consistent field, the internal consistency being described by the fundamental equations of dynamical theory (Authier, 2005),

$$\mathbf{D}_p = \frac{(\mathbf{k}_p)^2}{(\mathbf{k}_p)^2 - K^2} \sum_q \chi_{p-q} \mathbf{D}_{q[p]}. \quad (3)$$

$\mathbf{D}_{q[p]}$ represents the projection of the vector amplitude $\mathbf{D}_q$ on a plane perpendicular to the wavevector $\mathbf{k}_p$, $\mathbf{k}_p = \mathbf{k}_o + \mathbf{p}$, with $\mathbf{p}$ being a reciprocal-lattice vector. $\mathbf{k}_o$ is the wavevector of the forward-transmitted field. $K = 1/\lambda$ is the wavenumber in vacuum, $\nu = cK$ the frequency and c is the velocity of light. The elements $\{\chi_p\}$ are the coefficients in the Fourier series of the electrical susceptibility,

$$\chi_p = -\frac{r_e \lambda^2}{\pi V_c} F_p, \quad (4)$$

with r_e being the classical electron radius, V_c the unit-cell volume and F_p the structure factor associated with the reciprocal-lattice node p. The quadratic nature of the denominator of the resonance term,

$$\frac{(\mathbf{k}_p)^2}{(\mathbf{k}_p)^2 - K^2},$$

implies that only lattice nodes very close to the Ewald sphere will give rise to waves with considerable amplitudes.

2.2. Scalar representation

Maxwell's equation, $\nabla \cdot \mathbf{D} = 0$, implies that the displacement field is transverse. Using local coordinate systems defined by the unit-vector triplets, $\mathbf{e}_p^\mu \in \{\boldsymbol{\sigma}_p, \boldsymbol{\pi}_p, \mathbf{u}_p\}$ with $\boldsymbol{\sigma}_p \times \boldsymbol{\pi}_p = \mathbf{u}_p$ and $\mathbf{u}_p = \mathbf{k}_p/|\mathbf{k}_p|$, the individual vector amplitudes may be decomposed according to

$$\mathbf{D}_p = \sum_{\mu=1}^{2} D_p^\mu \mathbf{e}_p^\mu.$$

Following Weckert & Hümmer (1997),

$$\boldsymbol{\pi}_p = \frac{\mathbf{u}_p \times \mathbf{n}_{oh}}{|\mathbf{u}_p \times \mathbf{n}_{oh}|},$$

where

$$\mathbf{n}_{oh} = \frac{\mathbf{u}_h \times \mathbf{u}_o}{|\mathbf{u}_h \times \mathbf{u}_o|}$$

is a reference unit vector perpendicular to the primary diffraction plane. Thus all elements $\{\boldsymbol{\pi}_p\}$ are parallel to this plane.

The vector equations (3) are then replaced by the scalar equations

$$\left[\frac{(\mathbf{k}_p)^2 - K^2}{(\mathbf{k}_p)^2} - \chi_0\right] D_p^\mu - \sum_{q \neq p} \sum_\tau \chi_{p-q} (\mathbf{e}_p^\mu \cdot \mathbf{e}_q^\tau) D_q^\tau = 0. \quad (5)$$

2.3. Resonance error, *Anpassung* and excitation error[1]

In this work, we will avoid extreme geometries where the full set of solutions for equation (5) is needed. Thus we apply the linearization scheme (Pinsker, 1978)

[1] The literature offers different definitions and notations of various deviation parameters within the field of diffraction physics. Over the years, we have adopted a 'language' somewhat in between Authier (2005) and Cowley (1990). Thus it becomes an important task to give explicit definitions of all quantities that are introduced.

$$\left[\frac{(\mathbf{k}_p)^2 - K^2}{(\mathbf{k}_p)^2} - \chi_0\right] \approx 2\frac{\beta_p}{K},$$

where β_p, called the resonance error, is defined by

$$\beta_p = \|\mathbf{k}_p\| - k. \tag{6}$$

$k = K(1 + \chi_o/2)$ is the average wavenumber within the crystal. The kinematical boundary condition, which links the wavevector $\mathbf{k}_o$ to the incoming vacuum wavevector, $\mathbf{K}_o$, is expressed by

$$\mathbf{k}_o = \mathbf{K}_o - K\delta\mathbf{n}_e. \tag{7}$$

$\mathbf{n}_e$ is a unit vector perpendicular to the crystal entrance surface directed into the crystal and we denote the *Anpassung* as δ. To first order, we have

$$\|\mathbf{k}_p\| = \|\mathbf{K}_p\| - K\delta\gamma_p.$$

$\mathbf{K}_p = \mathbf{K}_o + \mathbf{p}$ and the direction cosine, γ_p, is expressed by $\gamma_p = \mathbf{n}_e \cdot (\mathbf{K}_p/K)$. At this point, it is convenient to introduce the excitation error, α_p, defined by the equation

$$\alpha_p = \|\mathbf{K}_p\| - K. \tag{8}$$

It measures the shortest distance from lattice node p to the surface of the Ewald sphere, *i.e.* along an Ewald-sphere radius. The three key quantities are coupled by

$$\beta_p = \alpha_p - K\delta\gamma_p - \tfrac{1}{2}K\chi_o. \tag{9}$$

2.4. Working equations

Combing equations (2) and (7), we obtain an expansion for the Ewald wave in a basis of vacuum plane waves,

$$\mathbf{D}(\mathbf{r}, t) = \sum_{\mu=1}^{2}\sum_{p=1}^{n} d_p^\mu \mathbf{e}_p^\mu \exp[2\pi i(\nu t - \mathbf{K}_p \cdot \mathbf{r})],$$

with

$$d_p^\mu = D_p^\mu \exp[i(2\pi K\delta)z]. \tag{10}$$

$z = (\mathbf{r} \cdot \mathbf{n}_e)$ measures the depth beneath the entrance surface of the crystal. We define the symbol subequations:

$$\Lambda = \quad 2\pi K\delta, \tag{11a}$$

$$b_p = -\frac{\pi K\chi_0}{|\gamma_p|} = \frac{r_e\lambda}{|\gamma_p|V_c}F_0, \tag{11b}$$

$$a_p = \quad \frac{2\pi\alpha_p}{|\gamma_p|}, \tag{11c}$$

$$\eta_{pq}^{\mu\tau} = -\frac{\pi K\chi_{p-q}}{|\gamma_p|}(\mathbf{e}_p^\mu \cdot \mathbf{e}_q^\tau) = \frac{r_e\lambda}{|\gamma_p|V_c}F_{p-q}(\mathbf{e}_p^\mu \cdot \mathbf{e}_q^\tau). \tag{11d}$$

The fundamental equations, equation (5), are then expressed by

$$\Lambda D_p^\mu = S(\gamma_p)\left[(b_p + a_p)D_p^\mu + \sum_{q\neq p}\sum_{\tau}\eta_{pq}^{\mu\tau}D_q^\tau\right], \tag{12}$$

where $S(\gamma_p)$ is the sign of the direction cosine γ_p. For Laue beams, $S(\gamma_p) = +1$ and, for Bragg beams, $S(\gamma_p) = -1$.

2.5. Excitation error revisited

The situation with a monochromatic incoming plane wave and an idealized crystal having a lattice-node density in reciprocal space (**K** space) modeled by an infinite set of Dirac δ functions, $\sum_q \delta(\mathbf{K} - \mathbf{q})$, is never encountered. The sum spans an infinite number of reciprocal-lattice vectors $\mathbf{q}$. The incoming beam inevitably has a certain divergence and wavelength spread modeled by the change $\Delta\mathbf{K}_o$ with respect to the geometrical wavevector $\mathbf{K}_o$. For real 'mosaic' crystals, the lattice-node density should be represented by distributions $\sum_q W(\mathbf{K} - \mathbf{q})$. If the reciprocal-lattice vector $\mathbf{p}$ satisfies the kinematical Bragg condition for the ideal case, we are now left with an intrinsic deviation, $\Delta\mathbf{p}_i$. Furthermore, there might be a deliberate deviation, $\Delta\mathbf{p}_e$, brought about by the action of the goniometer. The latter quantity is represented by infinitesimal rotations about some axes, $\boldsymbol{\varepsilon} \in (\boldsymbol{\omega}, \boldsymbol{\psi})$, *i.e.* $\Delta\mathbf{p}_e = (\boldsymbol{\varepsilon} \times \mathbf{p})\Delta\varepsilon$. $\boldsymbol{\omega}$ is oriented perpendicular to the primary diffraction plane and $\boldsymbol{\psi}$ is along the primary reciprocal-lattice vector. The general expression for the excitation error then becomes

$$\begin{aligned}\alpha_p &= \|\mathbf{K}_o + \Delta\mathbf{K}_o + \mathbf{p} + \Delta\mathbf{p}\| - K\left(1 - \frac{\Delta\lambda}{\lambda}\right)\\ &\approx \frac{\Delta\mathbf{K}_o \cdot \mathbf{p} + \mathbf{K}_o \cdot \Delta\mathbf{p}_e + \mathbf{K}_p \cdot \Delta\mathbf{p}_i}{K}.\end{aligned} \tag{13}$$

The actual deviations are written as

$$\begin{aligned}\Delta\mathbf{K}_o &= K[\Delta\kappa_1\boldsymbol{\sigma}_o + \Delta\kappa_2\boldsymbol{\pi}_o - (\Delta\lambda/\lambda)\mathbf{u}_o],\\ \Delta\mathbf{p}_e &= (\boldsymbol{\omega} \times \mathbf{p})\Delta\omega + (\boldsymbol{\psi} \times \mathbf{p})\Delta\psi.\end{aligned}$$

Here, $\Delta\kappa_1$ and $\Delta\kappa_2$ measure the vertical and horizontal divergence, respectively. $\boldsymbol{\omega}$ and $\boldsymbol{\psi}$ are orthogonal axes and their contributions may be summed independently. Thus the excitation error is built from

$$\alpha_p = \alpha_p^{(0)} + \alpha_p^{(\omega)} + \alpha_p^{(\psi)} + \alpha_p^{(i)}$$

and explicitly

$$\alpha_p^{(0)} = \Delta\kappa_1(\boldsymbol{\sigma}_o \cdot \mathbf{u}_p) + \Delta\kappa_2(\boldsymbol{\pi}_o \cdot \mathbf{u}_p) + (\Delta\lambda/\lambda)(1 - \mathbf{u}_o \cdot \mathbf{u}_p), \tag{14a}$$

$$\alpha_p^{(\omega)} = [1/(\lambda \sin 2\theta_{oh})]\{\mathbf{u}_p \cdot [\mathbf{u}_o \times (\mathbf{u}_o \times \mathbf{u}_h)]\}\Delta\omega, \tag{14b}$$

$$\alpha_p^{(\psi)} = [1/(2\lambda \sin\theta_{oh})][\mathbf{u}_p \cdot (\mathbf{u}_o \times \mathbf{u}_h)]\Delta\psi, \tag{14c}$$

$$\alpha_p^{(i)} = \mathbf{u}_p \cdot \Delta\mathbf{p}_i. \tag{14d}$$

Here $2\theta_{oh} = \measuredangle(\mathbf{K}_o, \mathbf{K}_h)$, $\Delta\omega = (\omega - \omega_0)$ and $\Delta\psi = (\psi - \psi_0)$, where ω_0 and ψ_0 are reference positions calculated from an average crystallographic metric. Crystal imperfections may be modeled by distributions in these parameters. Thus the term in equation (14*d*) may be embedded in equations (14*b*) and (14*c*) leaving us with a broadening procedure handled by relevant convolution integrals (Weckert & Hümmer, 1997). Equation (14*a*) may be combined with equations (14*b*) and (14*c*) to evaluate the effect of beam divergence and wavelength dispersion with respect to the angular distributions of the diffracted beams.

2.6. Method of solution

The crystal geometry adopted for this theoretical review is a semi-infinite parallel slab of thickness t. Thus no lateral boundaries need to be considered. Equation (12) may be formally written as

$$\Lambda|D\rangle = A|D\rangle. \tag{15}$$

A is the 'system' matrix. The ket, $|D\rangle$, is a column vector of the scalar amplitudes arranged as follows:

$$|D\rangle = \begin{pmatrix} D_o^\sigma \\ D_h^\sigma \\ D_g^\sigma \\ \vdots \\ D_n^\sigma \\ D_o^\pi \\ D_h^\pi \\ \vdots \\ D_n^\pi \end{pmatrix}.$$

Equation (15) represents an eigenvalue problem, and we use the symbol $|v_i\rangle$ for the eigenvector associated with the eigenvalue Λ_i,

$$|v_i\rangle = \begin{pmatrix} v_{oi}^\sigma \\ v_{hi}^\sigma \\ v_{gi}^\sigma \\ \vdots \\ v_{ni}^\sigma \\ v_{oi}^\pi \\ v_{hi}^\pi \\ \vdots \\ v_{ni}^\pi \end{pmatrix}.$$

The amplitude vector of the elements $\{d_p^\mu\}$ in equation (10) generally becomes

$$|d\rangle = \sum_{i=1}^{2n} w_i \exp(i\Lambda_i z)|v_i\rangle.$$

w_i is the weight or excitation coefficient of mode i. The weights are determined from the dynamical boundary conditions. In the present scheme of simplifications, these conditions, continuity of $\mathbf{D}_\perp$ and $\mathbf{E}_\parallel$ (the parallel component of the electrical field vector) across the crystal surfaces, are replaced by continuity of $\mathbf{D}$. Specularly reflected waves at the entrance surface are neglected. We write

$$\begin{aligned} &\mathbf{D}_o(z=0) = D_0^\sigma \boldsymbol{\sigma}_o + D_0^\pi \boldsymbol{\pi}_o, \\ &\mathbf{D}_p(z=0) = 0 \quad p \in \{\text{Laue beams}\}, \quad p \neq o, \\ &\mathbf{D}_p(z=t) = 0 \quad p \in \{\text{Bragg beams}\}. \end{aligned}$$

To handle the boundary conditions efficiently, we introduce the following notation:

$$z_p = (0 \vee t) \Leftrightarrow \bar{z}_p = (t \vee 0) \quad p \in \{o, h, g, \ldots, n\},$$

remembering that the entrance surface and the exit surface will always be opposite pairs, located at $z = 0 \vee t$, for all beams $\mathbf{K}_p$. At the entrance, the actual amplitude vector, denoted by $|d_0\rangle$, becomes

$$|d_0\rangle = \begin{pmatrix} D_0^\sigma \\ 0 \\ 0 \\ \vdots \\ 0 \\ D_0^\pi \\ 0 \\ \vdots \\ 0 \end{pmatrix}.$$

The boundary conditions may be compactly formulated by introducing the matrices ($\otimes$ indicates a direct product)

$$T_i = \operatorname{diag}\big(\exp(i\Lambda_i z_o), \exp(i\Lambda_i z_h), \exp(i\Lambda_i z_g), \ldots, \exp(i\Lambda_i z_n)\big) \otimes \operatorname{diag}(1,1)$$

and

$$S = [T_1|v_1\rangle\ T_2|v_2\rangle \ldots T_{2n}|v_{2n}\rangle].$$

Thus at the entrance surface we have

$$S|w\rangle = |d_0\rangle,$$

giving the excitation coefficient vector

$$|w\rangle = S^{-1}|d_0\rangle. \tag{16}$$

Furthermore, defining the 'conjugated' matrices

$$\overline{T}_i = \operatorname{diag}\big(\exp(i\Lambda_i \bar{z}_o), \exp(i\Lambda_i \bar{z}_h), \exp(i\Lambda_i \bar{z}_g), \ldots, \exp(i\Lambda_i \bar{z}_n)\big) \otimes \operatorname{diag}(1,1)$$

and

$$\overline{S} = \big[\overline{T}_1|v_1\rangle\ \overline{T}_2|v_2\rangle \ldots \overline{T}_{2n}|v_{2n}\rangle\big],$$

we obtain the amplitude vector at the exit, denoted by $|d_e\rangle$, as

$$|d_e\rangle = \overline{S}|w\rangle = \overline{S}S^{-1}|d_0\rangle. \tag{17}$$

For an incoming beam of unit power, the intrinsic power for a diffracted beam in the direction given by $\mathbf{K}_p$ (Laue transmitted or Bragg reflected) becomes

$$P_p = \frac{|\gamma_p|}{\gamma_o} \sum_\mu |(d_e)_p^\mu|^2. \tag{18}$$

The effect of distributions in the experimental parameters entering equations (14) may finally be accommodated by appropriate convolutions to yield simulations to be compared with the measured three-beam profiles.

2.7. Anomalous scattering factors

The diffracted power, as given in equation (18), will be sensitive to resonance conditions *via* the wavelength dependence of the coupling factors, $\eta_{pq}^{\mu\tau}$. These are directly proportional to the structure factor, F_{p-q} [consult equation (11d)]. To model the resonant scattering associated with the K edge of germanium, we have primarily used anomalous scattering factors as provided by Cromer & Liberman (1970, 1981) and

made available by the program *FPRIME* (Cromer, 1983, 1995). Their method is based on the dipole approximation and includes relativistic effects. Cross sections are calculated from Dirac–Slater wavefunctions and the Kramers–Kronig relations are applied to derive f' from calculated values of f''. The influence of the resonance terms on an arbitrary coupling factor is shown in Fig. 1. It should be noted that readily accessible experimental values for Ge seem to be scarce but Fig. 1 of Schülli *et al.* (2003) could be consulted. In general, the literature (Begum *et al.*, 1986; Fukamachi *et al.*, 1990; Creagh, 1991; Creagh & McAuley, 1995) points especially to challenges in accurately predicting f' very close to the K threshold. Therefore, we have also evaluated results based on an approach using second-order scattering-matrix theory (Kissel *et al.*, 1980, 1995). Here, a relativistic Hartree–Fock–Slater potential with a Latter tail was used to obtain a tabulation of f' and f'' for germanium between 5 and 25 keV (Kissel, 1995).

3. Experimental

A thin sample of germanium had been prepared from a single crystal and etched normal to the $[\bar{1}10]$ direction, yielding an average thickness of approximately 15 µm. From this foil, small pieces were cut and glued onto short capillary glass spikes. The experiments were carried out at the Swiss–Norwegian beamlines (SNBL, BM01A) at ESRF. This bending-magnet beamline was set up for parallel-beam optics – that is a double Si(111) monochromator with a flat second crystal. The energy resolution of the monochromatic beam is $\Delta\lambda/\lambda \approx 1.4 \times 10^{-4}$ and the beam divergences are approximately 25 µrad both horizontally and vertically. The incident-beam cross section was defined by the post-monochromator slits in such a way that it was 540×540 µm at the diffractometer position. The wavelength was initially calibrated using a known reflection from a small perfect-silicon-crystal sample. All measurements were performed at room temperature. Crystals were mounted on the special high-precision ψ-circle HUBER diffractometer (Hümmer *et al.*, 1987) with the steering software system *diff6* (Weckert & Hümmer, 1997). Their quality was checked by performing two-beam ω scans. It turned out that most of the samples had to be rejected because of too high a degree of imperfection. Several showed signs of mosaic block formation, however one single-crystal fragment yielded acceptable homogeneous peaks. Fig. 2 displays the experimental and the theoretical rocking curve for reflection $\bar{1}\bar{1}\bar{3}$. Generally, the FWHM of the chosen primary reflections spans the range $(4.5, 10.0) \times 10^{-3}$ degrees. The slightly idealized shape of the crystal used for the investigations is shown in Fig. 3. Since the wavelength calibration has a finite uncertainty, the absorption K edge of the sample was determined experimentally by measuring the fluorescence yield. The result is depicted in Fig. 4. 16 reflections with $2\theta \in (21, 84^\circ)$ were collected to build the orientation matrix. A joint refinement of orientation matrix and metric, the latter constrained to the

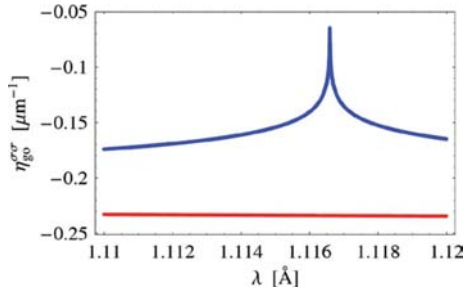

Figure 1
The real part of the coupling factor $\eta_{go}^{\sigma\sigma}$ for the three-beam case $224/\bar{2}24/400$ in germanium depicted as a function of wavelength. Red: without contribution from resonance scattering terms. Blue: with inclusion of f' and f'' from the Cromer–Liberman analysis.

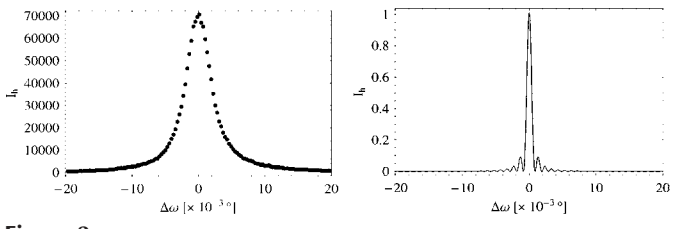

Figure 2
Measured (left) and simulated (right) rocking curves for reflection $\bar{1}\bar{1}\bar{3}$ in germanium for a horizontal scattering configuration. The actual wavelength is $\lambda = 1.1200$ Å. The simulation is for a plate thickness $t = 11.5$ µm. The FWHMs are (4.5×10^{-3}) and $(0.7 \times 10^{-3})^\circ$, respectively.

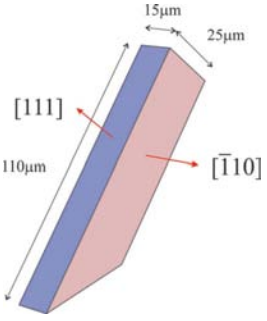

Figure 3
Schematic picture of the germanium crystal showing actual dimensions and crystallographic directions.

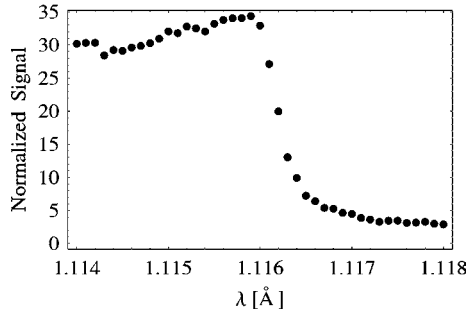

Figure 4
Fluorescence signal (counts s^{-1}) as a function of wavelength across the K-absorption edge. Each point is the average of three repetitions (obtained by stepping ϕ by 0.01°). The signal has been scaled by the monitor counts and the counting time per measurement was 60 s. The point of inflection occurs approximately at $\lambda = 1.1161$ Å. Compared to the Cromer–Liberman resonance data ($\lambda_K \approx 1.1166$ Å), this indicates a systematic error in the wavelength of ≈ 0.0005 Å. The analysis of the crystallographic metric confirms this result.

cubic crystal system, resulted in a lattice parameter $a = 5.6557\,(2)$ Å (assuming negligible wavelength spread). Comparing this result with the one given by Hom *et al.* (1975), $\langle a \rangle = 5.657820$ Å, indicates a systematic error in the wavelength of approximately 0.0005 Å in accordance with the fluorescence yield measurements. The shift in wavelength probably reflects a minor error in the calibration of the monochromator at the time of the experiments. Five pairs of Friedel-equivalent ψ-scan profiles and a single one were measured as a function of wavelength, nine values in the range (1.1100, 1.1200) Å, with additional reference measurements at $\lambda = 1.0000$ and $\lambda = 1.2000$ Å. Fig. 5 depicts the resonance scattering factors for germanium in the actual wavelength range. For each wavelength, the primary and secondary reflections were re-centered in order to get an accurate determination of the exact three-beam point position (ω_0, ψ_0). This local optimization ensures that the ψ scan is performed at the top of the two-beam ω rocking curve. ψ curves were obtained by angular scans having a fixed width of 0.2° divided into 400 steps of $(0.5 \times 10^{-3})^\circ$. The unperturbed two-beam level was then recovered at both ends of the scan interval. For the Laue-transmission cases where the two-beam ridge has a symmetrical appearance, *cf.* Fig. 6, the elaborate centering procedures warrant an accurate experimental three-beam profile. An alternative approach, utilizing a combined ω/ψ-step scan, may cause an unwanted broadening of the ψ profiles, *cf.* Thorkildsen (1987) and Mo *et al.* (1998). As pointed out by Shen (1993), the natural beam divergence will inherently provide a partial ω integration. A plastic (point) scintillator counter was used. The detector window was chosen large enough to give an appropriate instrumental integration

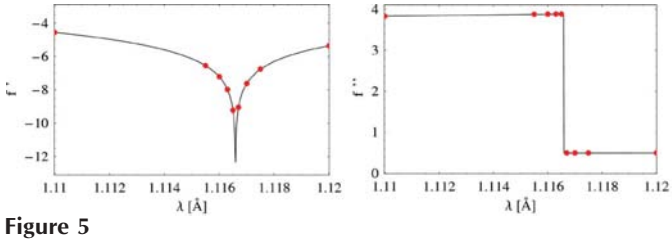

Figure 5
Resonance scattering factors for germanium after Cromer & Liberman, real (f') and imaginary (f'') parts. The red points indicate the actual wavelengths (corrected for the systematic error) used for the measurements.

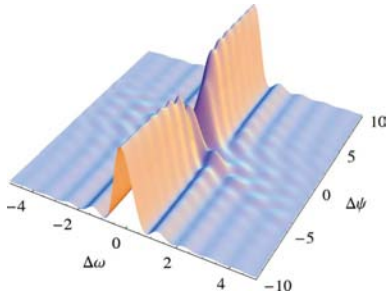

Figure 6
Three-beam three-dimensional profile for the case $\bar{1}\bar{1}\bar{3}/\bar{2}\bar{2}0/11\bar{3}$ calculated for a crystal thickness $t = 10$ µm and a wavelength $\lambda = 1.1100$ Å. $\Delta\omega$ and $\Delta\psi$ in thousandths of a degree.

Table 1
Simulating the FWHM, $\Delta\omega_e$, of the experimental rocking curves, *cf.* Fig. 2, for the primary reflections of the three-beam cases depicted in Figs. 7–10.

Contributions are due to the intrinsic width of the reflection, $\Delta\omega_i$, dispersion, $\Delta\omega_d$ and mosaic spread, $\Delta\omega_m$. The latter quantity is calculated based on the Gaussian assumption of quadratic summation of individual terms, $\Delta\omega_e^2 = \Delta\omega_i^2 + \Delta\omega_d^2 + \Delta\omega_b^2 + \Delta\omega_m^2$. $\Delta\omega_b = (1.5 \times 10^{-3})^\circ$ is due to beam divergence. All values are given in thousandths of a degree. Apart from the intrinsic widths, all values are rounded to within $(0.5 \times 10^{-3})^\circ$. Data are for $\lambda = 1.1200$ Å.

h	$\Delta\omega_e$	$\Delta\omega_i$	$\Delta\omega_d$	$\Delta\omega_m$
$\bar{1}\bar{1}\bar{3}$	4.5	0.70	3.0	3.0
$\bar{1}\bar{1}\bar{5}$	7.0	0.55	5.0	5.0
$\bar{1}\bar{1}\bar{1}$	8.0	1.65	1.5	7.5
$\bar{1}\bar{3}\bar{5}$	10.0	0.25	6.0	8.0

providing data comparable to simulations that take a finite beam divergence into account. The results presented are averages of ten or more subsequently repeated scans, ensuring proper counting statistics. The signal-to-noise ratio is worse for wavelengths just below the K edge. This was partly compensated for by an increase in accumulated counting time. Separate calculations were performed in order to verify that no other interfering neighboring lattice nodes were present within the scan interval.

4. Results and discussion

Four experimental three-beam profiles, presented as the relative change in the diffracted power with respect to the corresponding two-beam level, $\Delta\mathcal{P}_h/\mathcal{P}_h$, for nine different values of the wavelength[2] are shown in Figs. 7– 10. Owing to different parameter combinations, they cover various appearances of three-beam perturbations. All three-beam profiles are arranged such that a positive value of $\Delta\psi$ corresponds to a position of the secondary reciprocal-lattice node inside the Ewald sphere. The figures also illustrate the beam paths through the crystal (as calculated for $\lambda = 1.200$ Å), the wavelength dependence of the coupling parameters, $\eta_{pq}^{\pi\pi}$, and the results of the simulations. The three-beam profiles chosen all have beam paths that may be approximately associated with a single entrance surface and are classified as Laue–Laue cases. Table 1 gives a summary of the analysis of the rocking-curve measurements of the associated primary reflections. It is evident that there is a broadening of the reflections that may be attributed to mosaicity. To simulate the experimental profiles, convolution integrals are introduced to take this feature into account. From the point of view of the calculations, broadening may be empirically linked to beam divergence that has been modeled by a product of two identical Pearson VII functions[3] (Snyder *et al.*, 1999) in the variables $\Delta\kappa_1$ and $\Delta\kappa_2$, Pearson VII index $m = 2$. The simulated profiles are hence obtained by a two-dimensional-numerical

[2] Actual wavelengths are λ = 1.1100, 1.1150 (simulated only), 1.1155, 1.1160, 1.1163 (measured only), 1.1165, 1.1167, 1.1170, 1.1175, 1.1180 (simulated only) and 1.1200 Å.
[3] The Pearson VII function, $\Xi(x)$, is defined by $\Xi(x) = \Xi(0)[1/(1 + Cx^2)^m]$ with $C = (2^{1/m} - 1)/(\Delta/2)^2$.

convolution procedure. The ranges of integration are $\pm 2\Delta$, where Δ is the FWHM of the Pearson VII functions. Wavelength dispersion is thus embedded into the description of the divergence and it is assumed that beam angular broadening owing to crystal imperfection is covered by this procedure too. Δ is treated as an adjustable parameter. A semi-infinite slab is still kept as the geometrical model for the simulations. However, for the same reason as above, the dynamical block size, t, is treated as a free parameter, $t \leq T$, the measurable crystal thickness. Generally, owing to its finiteness and being

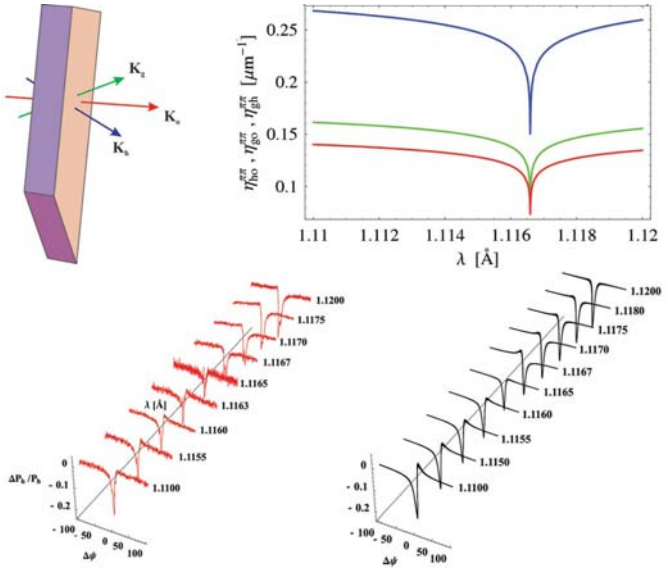

Figure 7
Three-beam case $\bar{1}\bar{1}\bar{3}/\bar{2}\bar{2}0/11\bar{3}$. Upper left: beam paths through the crystal illustrated by their wavevectors. Upper right: coupling parameters among the waves. The figure shows the absolute value of the real part of $\eta_{pq}^{\pi\pi}$. $pq \in oh$ (red), og (blue) and gh (green). Lower left: experimental three-beam profiles. Lower right: simulated profiles; dynamical block size $t = 11.5$ µm, $\Delta = (6.0 \times 10^{-3})^\circ$. $\Delta\psi$ is given in thousandths of a degree. The actual wavelengths indicated are valid for Figs. 8–10 as well.

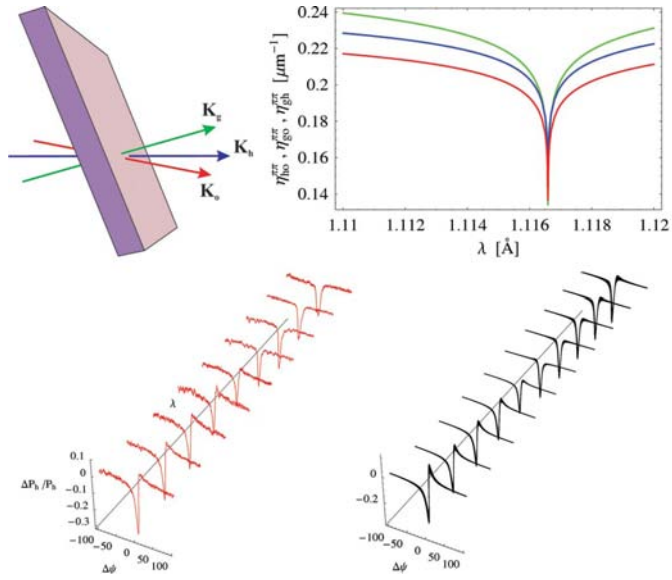

Figure 9
Three-beam case $\bar{1}1\bar{1}/11\bar{1}/\bar{2}\bar{2}0$. Upper left: beam paths through the crystal illustrated by their wavevectors. Upper right: coupling parameters among the waves. The figure shows the absolute value of the real part of $\eta_{pq}^{\pi\pi}$. $pq \in oh$ (red), og (blue) and gh (green). Lower left: experimental three-beam profiles. Lower right: simulated profiles; dynamical block size $t = 8.5$ µm, $\Delta = (5.0 \times 10^{-3})^\circ$. $\Delta\psi$ is given in thousandths of a degree.

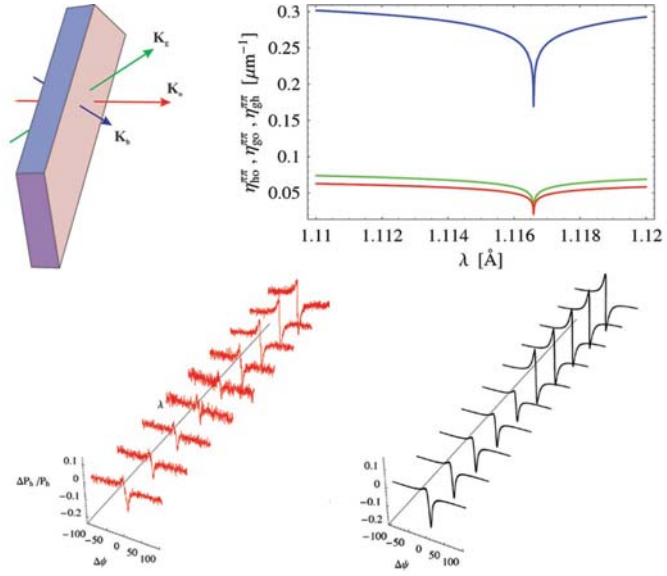

Figure 8
Three-beam case $\bar{1}1\bar{5}/\bar{2}\bar{2}0/11\bar{5}$. Upper left: beam paths through the crystal illustrated by their wavevectors. Upper right: coupling parameters among the waves. The figure shows the absolute value of the real part of $\eta_{pq}^{\pi\pi}$. $pq \in oh$ (red), og (blue) and gh (green). Lower left: experimental three-beam profiles. Lower right: simulated profiles; dynamical block size $t = 10.0$ µm, $\Delta = (6.0 \times 10^{-3})^\circ$. $\Delta\psi$ is given in thousandths of a degree.

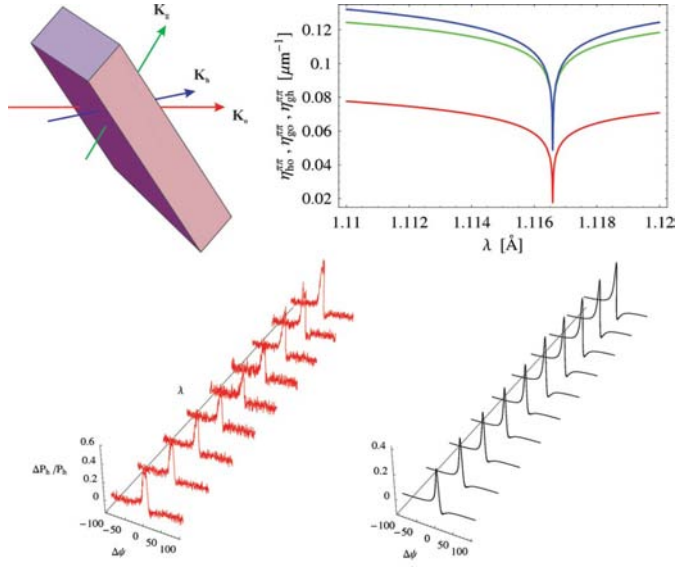

Figure 10
Three-beam case $\bar{1}3\bar{5}/\bar{4}\bar{2}\bar{2}/3\bar{1}\bar{3}$. Upper left: beam paths through the crystal illustrated by their wavevectors. Upper right: coupling parameters among the waves. The figure shows the absolute value of the real part of $\eta_{pq}^{\pi\pi}$. $pq \in oh$ (red), og (blue) and gh (green). Lower left: experimental three-beam profiles. Lower right: simulated profiles; dynamical block size $t = 9.0$ µm, $\Delta = (6.0 \times 10^{-3})^\circ$. $\Delta\psi$ is given in thousandths of a degree.

Table 2
Average path lengths l_p [μm] along the beam directions $\mathbf{K}_p$, $p \in \{o, h, g\}$, and appropriate direction cosines, γ_p, for the three-beam cases, as calculated for $\lambda = 1.110$ Å.

$\mathbf{h}/\mathbf{g}/\mathbf{h}-\mathbf{g}$	l_o	l_h	l_g	γ_o	γ_h	γ_g
$\bar{1}\bar{1}\bar{3}/\bar{2}\bar{2}0/11\bar{3}$	15	15	16	0.933	0.933	0.933
$\bar{1}\bar{1}5/\bar{2}\bar{2}0/11\bar{5}$	15	16	17	0.848	0.848	0.848
$\bar{1}\bar{1}\bar{1}/11\bar{1}/\bar{2}\bar{2}0$	15	15	15	0.956	0.956	0.956
$\bar{1}\bar{3}\bar{5}/\bar{4}\bar{2}\bar{2}/3\bar{1}\bar{3}$	18	27	15	0.668	0.390	0.945

completely bathed in the X-ray beam, a single well defined length characterizing the crystal does not exist. The best overall values for the model parameters, t and Δ, were determined by a trial-and-error approach repeating the calculations for various combinations of these quantities. The simulated profiles are built from 21 individual simulations across the FWHM of the underlying two-beam rocking curves (by stepping $\Delta\omega$).

In the model simulations, the incoming beam is assumed to be 100% polarized in the horizontal plane. Although not addressed in this particular experiment, the fraction of majority polarization, f_h, as given by Coppens (1992), was determined as 0.97 at a later stage (Thorkildsen, Larsen, Semmingsen & Bjaanes, 2001). A full simulation of the intrinsic three-beam profile for the $\bar{1}\bar{1}\bar{1}/11\bar{1}/\bar{2}\bar{2}0$ case, based on this value for f_h ($\lambda = 1.1167$ Å and $t = 7.5$ μm), resulted in a profile congruent to what was obtained with $f_h = 1.0$. The differences between the two simulations were less than 1% in the crucial parts of the profile (*cf.* Fig. 17). No attempt has been made to implement a variable random noise signal in the simulations. All calculations are performed by the software system *Mathematica* version 5.0 (Wolfram, 2003).

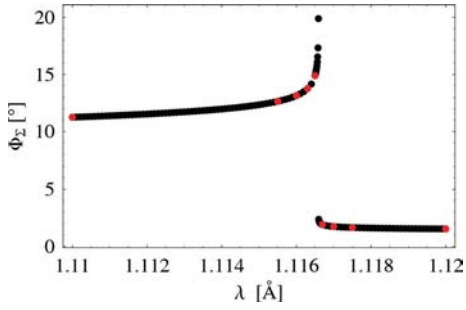

Figure 11
Triplet phase sum Φ_Σ as a function of wavelength for the three-beam case $\bar{1}\bar{1}\bar{3}/\bar{2}\bar{2}0/11\bar{3}$. Calculation based on Cromer–Liberman values for f' and f''.

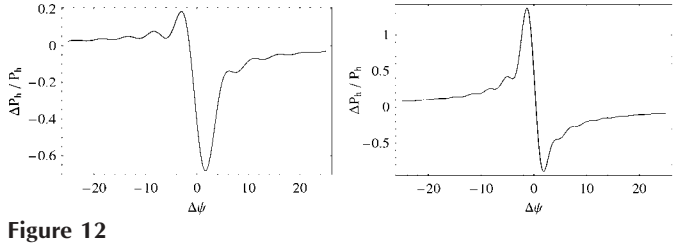

Figure 12
Generic intrinsic three-beam profiles for a triplet phase sum $\Phi_\Sigma = 0°$. Left: *Aufhellung* case. Right: *Umweganregung* case. $\Delta\psi$ is given in thousandths of a degree.

4.1. General comments

The overall agreement between simulations and experiments is quite astonishing. All major features may be well described by the fundamental theory of X-ray diffraction applying the Cromer–Liberman values for the resonance parameters. For the three-beam cases presented, the theoretical variation of the triplet phase sum Φ_Σ with wavelength has almost identical appearance as depicted in Fig. 11, *i.e.* $\Phi_\Sigma \approx 0°$. For this situation, we expect an intrinsic profile asymmetry typically as shown in Fig. 12. Thus one might be tempted to conclude that the experiments for the cases $\bar{1}\bar{1}\bar{3}/\bar{2}\bar{2}0/11\bar{3}$ and $\bar{1}\bar{1}\bar{1}/11\bar{1}/\bar{2}\bar{2}0$ indicate an error in the theoretical estimates for Φ_Σ. However, as mentioned in the *Introduction*, the profile shape for the Laue–Laue diffraction condition is critically dependent on the slab thickness. This is depicted in Fig. 13. Inverted asymmetries may be observed for very small thicknesses too. In transmission geometry, the expected three-beam profile behavior, *cf.* Fig. 6 in the article

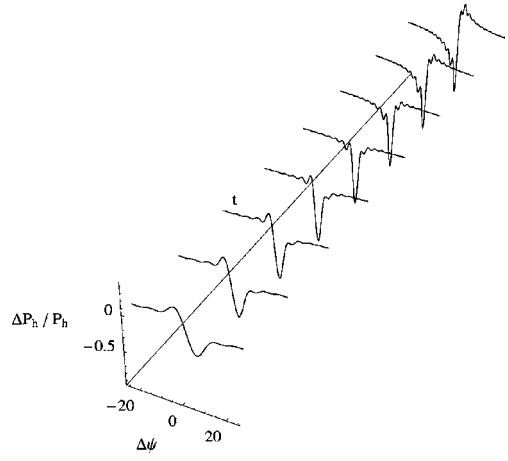

Figure 13
Intrinsic three-beam profiles for $\bar{1}\bar{1}\bar{1}/11\bar{1}/\bar{2}\bar{2}0$ as a function of the slab thickness t. $\lambda = 1.1100$ Å and $t = 2, 3, \ldots, 9$ μm.

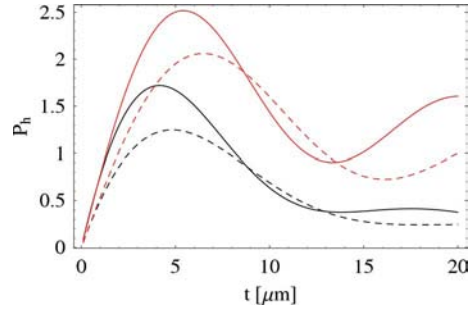

Figure 14
The intrinsic integrated two-beam power (arbitrary units) for $\bar{1}\bar{1}\bar{1}$ (diffraction in the horizontal plane) as a function of plate thickness revealing the *Pendellösung* behavior in Laue geometry. Black solid line: $\lambda = 1.1100$ Å. Black dashed line: $\lambda = 1.1165$ Å. Red dashed line: $\lambda = 1.1167$ Å. Red solid line: $\lambda = 1.1200$ Å.

by Weckert & Hümmer (1997), is reproduced when the slab thickness, or in the present case the dynamical block size, is not larger than the *Pendellösung* distance of the primary reflection of the actual triplet (Weckert & Hümmer, 1998). *Pendellösung* plots of the integrated power for the $\bar{1}\bar{1}\bar{1}$ reflection are shown in Fig. 14 for different wavelengths close to the *K* edge. Substantial variations are revealed. If the experimental conditions correspond to a position beyond the first maximum of the *Pendellösung*, inverted profiles may be observed. This is the case for the triplets $\bar{1}\bar{1}\bar{3}/\bar{2}\bar{2}0/11\bar{3}$ and $\bar{1}\bar{1}\bar{1}/11\bar{1}/\bar{2}\bar{2}0$ in this study. We consequently lean toward the opinion that the observed inverted profiles are an effect of the dynamical block size and as such not addressable to Φ_Σ. This feature is not easily explained by approximate diffraction theories (Shen & Huang, 2003; Thorkildsen, Larsen & Weckert, 2001) and may lead to misinterpretation of the value for the triplet phase sum. For the profiles presented, their Friedel partners come up with identical characteristics and thus support the conclusions drawn. Average path lengths, $l_p = (1/V)\int_v (T_p + T'_p)\,\mathrm{d}V$, with T_p measuring the distance from the entrance surface to the volume element $\mathrm{d}V$ and T'_p the distance from the same element to the exit surface, both measured along $\mathbf{K}_p$, are calculated along the same lines as the absorption factor by an analytical method (de Meulenaer & Tompa, 1965). The results are summarized in Table 2 together with appropriate direction cosines. It is a common feature that the crystal thickness (15 μm along $[\bar{1}10]$ of Fig. 3) exceeds the estimates of the dynamical block size most appropriate for fitting purposes. This fact is, as explained, associated with the crystal imperfection.

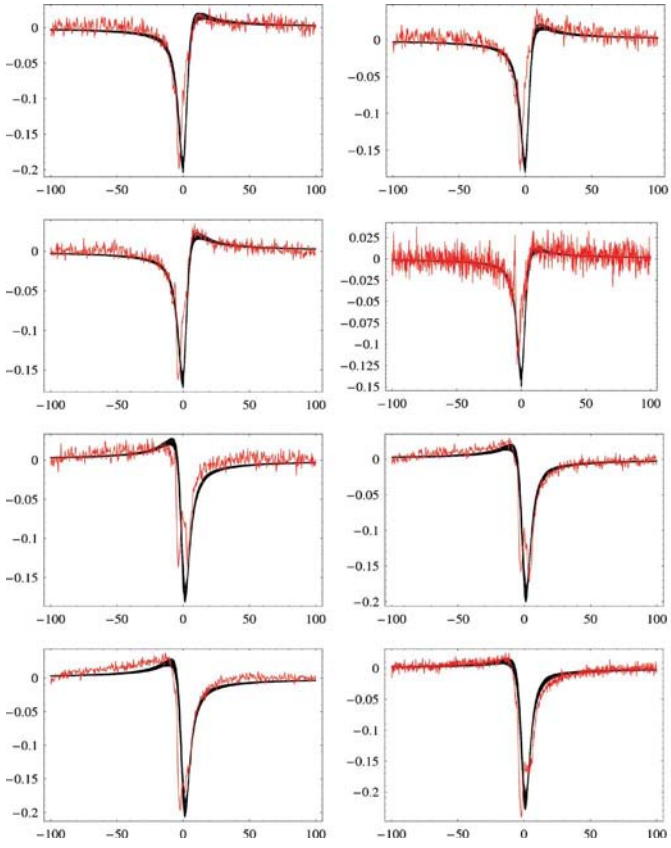

Figure 15
Best fit (black solid line) to experiments (in red) for the three-beam case $\bar{1}\bar{1}\bar{3}/\bar{2}\bar{2}0/11\bar{3}$. Increasing wavelength from upper left to lower right Actual dynamical block sizes applied in these simulations are summarized in Fig. 16. Abscissa: $\Delta\psi$ in thousandths of a degree. Ordinate: relative change in two-beam power.

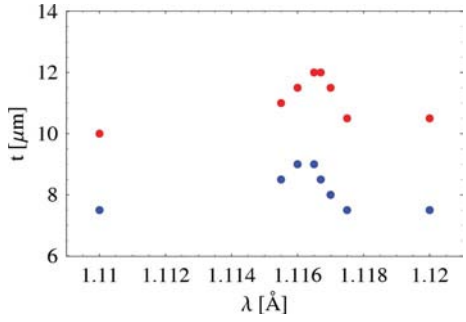

Figure 16
Most appropriate dynamical block size as a function of wavelength, revealed by comparison between simulations and experiments. Red: $\bar{1}\bar{1}\bar{3}/\bar{2}\bar{2}0/11\bar{3}$. Blue: $\bar{1}\bar{1}\bar{1}/11\bar{1}/\bar{2}\bar{2}0$.

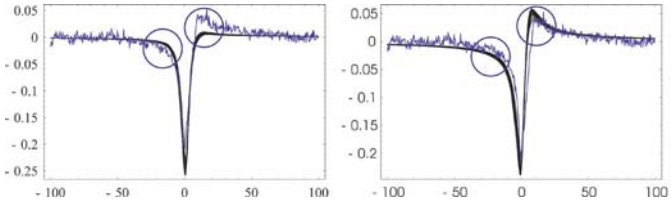

Figure 17
Three-beam case $\bar{1}\bar{1}\bar{1}/11\bar{1}/\bar{2}\bar{2}0$. The parts of a profile of greatest significance for assessment of the best fit have been encircled. Experiments at $\lambda = 1.1165$ Å. Dynamical block size used in the simulations are $t = 7.5$ and $t = 9.0$ μm for the left and right illustrations, respectively.

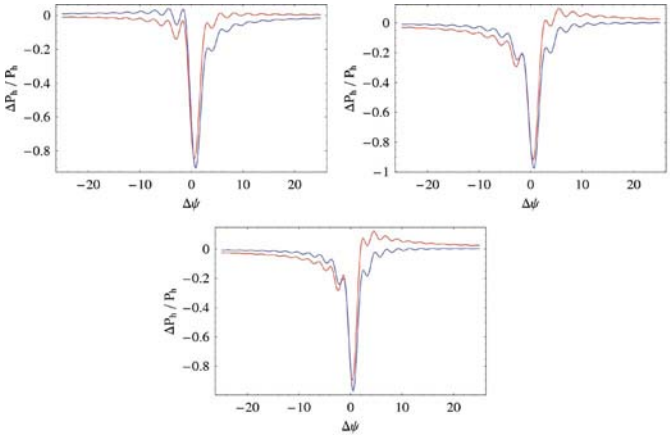

Figure 18
Intrinsic three-beam profiles for $\bar{1}\bar{1}\bar{1}/11\bar{1}/\bar{2}\bar{2}0$. Red: $\lambda = 1.1165$ Å. Blue: $\lambda = 1.1167$ Å. f' after Cromer & Liberman. Top left: $t = 7.5$ μm. Top right: $t = 7.5$ μm with f' reduced by a factor of 0.6. Bottom: $t = 9.0$ μm. A slab thickness of $t = 7.5$ μm gives the best fit at $\lambda = 1.110$ and 1.120 Å, while $t = 9.0$ μm is the optimum choice close to the resonance. $\Delta\psi$ is given in units of thousandths of a degree.

4.2. Details

The simulations were performed by increasing the dynamical block size in steps of 0.5 μm. It turned out that the best fits were obtained by different values of t for the various wavelengths. For the case $\bar{1}1\bar{3}/\bar{2}\bar{2}0/11\bar{3}$, this is illustrated in Fig. 15. An apparent increase in thickness close to λ_K is the common feature. A summary is depicted in Fig. 16, where we have also included the results for $\bar{1}\bar{1}1/11\bar{1}/\bar{2}\bar{2}0$. Fig. 17 indicates the parts of a profile we emphasize in particular when assessing goodness of fit by visual inspection. Since t should have a constant value, at least for a given three-beam case, this observation may indicate that another parameter of the scattering system is not properly described. A comparison of the Cromer–Liberman model with the Kissel model for the resonance parameters f' and f'' reveals the largest differences for f' in the vicinity of the resonance. Fig. 18 shows how changes in the main features of an intrinsic three-beam profile close to the K resonance owing to a thickness variation may be reproduced by reducing the value of f'. In the example presented, a factor of 0.6 was applied. We note that this seems to be in accordance with the adjustment of the high-energy limit of f' from the Cromer–Liberman calculations as indicated by Kissel *et al.* (1995). This may not be the final (and only) explanation, but at least indicates that three-beam diffraction in nearly perfect crystals may offer a very sensitive probe for resonance scattering effects.

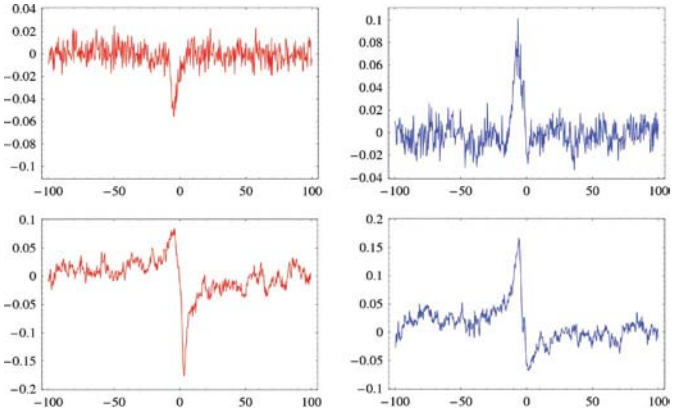

Figure 19
Experimental three-beam profiles – Friedel equivalents. Left: $\bar{2}\bar{2}4/2\bar{2}\bar{4}/\bar{4}00$. Right: $224/\bar{2}24/400$. Top row: $\lambda = 1.1160$ Å. Second row: $\lambda = 1.1170$ Å. Abscissa: $\Delta\psi$ in thousandths of a degree. Ordinate: relative change in the two-beam power.

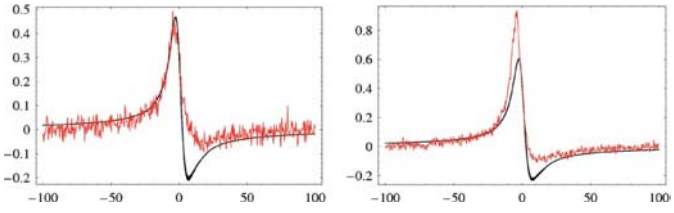

Figure 20
Three-beam case $440/13\bar{1}/311$. Left: $\lambda = 1.1160$ Å. Right: $\lambda = 1.1170$ Å. Simulations (black line) for $t = 7.0$ μm and $\Delta = (7.0 \times 10^{-3})^\circ$. Abscissa: $\Delta\psi$ in thousandths of a degree. Ordinate: relative change in the two-beam power.

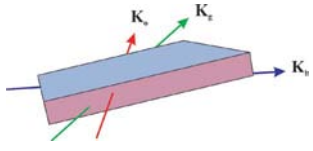

Figure 21
Three-beam case $440/13\bar{1}/311$, beam paths depicted relative to the actual finite crystal. Smallest take-off angle 2.27° for $\mathbf{K}_h$ with respect to face [111].

4.3. Challenges

Figs. 19 and 20 point out some peculiar results. In Fig. 19, large variations in the pair of Friedel three-beam profiles across the K edge are displayed. This may be attributed to different crystalline imperfection as encountered by the spatially reversed wavefields. Fig. 20 reveals a case where the 'best' simulations give subpar matching to the experimental points. For the actual three-beam case, the beam paths in the finite crystal, as illustrated in Fig. 21, are generally not compatible with the adopted model for simulation where the boundary conditions are specified with respect to a single pair of entrance and exit surfaces. These two aspects of the crystalline sample, its finite shape and its inherent state of imperfection, are the most intriguing ones both with respect to simulations and for correct interpretation of profile asymmetries.

5. Concluding remarks

Three-beam diffraction represents a very sensitive diffraction condition, revealing subtle details related to both coherent and incoherent scattering processes. In this paper, the focus has been on resonance scattering effects in conjunction with geometry. The examples presented confirm our opinion that three-beam diffraction is a versatile experimental method. We find it of great importance that various crystalline systems should be further investigated to fully explore its potential and its implications on future developments of diffraction theories.

The measurements were carried out at SNBL, ESRF, Experiment 01-02-43. We gratefully acknowledge the support from the SNBL staff and Dr I. Snigireva for providing the Ge crystal. This work has been supported by Norges Forskningsråd, Grant 129638/431.

References

Authier, A. (2005). *Dynamical Theory of X-ray Diffraction.* Oxford University Press. First published 2001, reprinted with revisions 2003, 2005.
Begum, R., Hart, M., Lea, K. R. & Siddons, D. P. (1986). *Acta Cryst.* A**42**, 456–464.
Chang, S.-L. (1982). *Phys. Rev. Lett.* **48**, 163–166.
Chang, S.-L. (1986). *Phys. Rev. B*, **33**, 5848–5850.
Chang, S.-L. (1992). *Int. J. Mod. Phys. B*, **6**, 2987–3020.
Colella, R. (1974). *Acta Cryst.* A**30**, 413–423.

Coppens, P. (1992). *Synchrotron Radiation Crystallography.* New York: Academic Press.
Cowley, J. M. (1990). *Diffraction Physics*, 2nd. ed. Amsterdam: North Holland.
Creagh, D. C. (1991). *Chin. J. Phys.* **29**, 299–325.
Creagh, D. C. & McAuley, W. J. (1995). In *International Tables for Crystallography*, Vol. C, edited by A. J. C. Wilson, pp. 206–222. Dordrecht: Kluwer Academic Publishers.
Cromer, D. (1983). *J. Appl. Cryst.* **16**, 437.
Cromer, D. (1995). Personal communication.
Cromer, D. & Liberman, D. (1970). *J. Chem. Phys.* **53**, 1891–1898.
Cromer, D. & Liberman, D. (1981). *Acta Cryst.* A**37**, 267–268.
Fukamachi, T., Yoshizawa, M., Ehara, K., Kawamura, T. & Nakajima, T. (1990). *Acta Cryst.* A**46**, 945–948.
Hom, T., Kiszenik, W. & Post, B. (1975). *J. Appl. Cryst.* **8**, 457–458.
Hümmer, K. & Billy, H. (1982). *Acta Cryst.* A**38**, 841–848.
Hümmer, K., Bondza, H. & Weckert, E. (1987). *Acta Cryst.* A**43**, C222.
Kissel, L. (1995). Private communication.
Kissel, L., Pratt, R. H. & Roy, S. C. (1980). *Phys. Rev. A*, **22**, 1970–2004.
Kissel, L., Zhou, B., Roy, S. C., Sen Gupta, S. K. & Pratt, R. H. (1995). *Acta Cryst.* A**51**, 271–288.
Kokubun, J., Ishida, K., Cabaret, D., Mauri, F., Vedrinskii, R. V., Kraizman, V. L., Novakovich, A. A., Krivitskii, E. V. & Dmitrienko, V. E. (2004). *Phys. Rev. B*, **69**, 2451031–24510313.
Kokubun, J., Ishida, K. & Dmitrienko, V. (1998). *J. Phys. Soc. Jpn*, **67**, 1291–1295.
Larsen, H. B. & Thorkildsen, G. (1998). *Acta Cryst.* A**54**, 129–136.
Larsen, H. B., Thorkildsen, G. & Weckert, E. (2005). *Acta Cryst.* A**61**, 134–138.
Lee, T. L., Felici, R., Hirano, K., Cowie, B., Zegenhagen, J. & Colella, R. (2001). *Phys. Rev. B*, **64**, 2013161–2013164.
Materlik, G., Sparks, C. J. & Fischer, K. (1994). *Resonant Anomalous X-ray Scattering: Theory and Applications.* Amsterdam: Elsevier.
Meulenaer, J. de & Tompa, H. (1965). *Acta Cryst.* **19**, 1014–1018.
Mo, F., Hauback, B. C., Mathiesen, R. H., Kvick, Å. & Weckert, E. (1998). *J. Synchrotron Rad.* **5**, 1369–1374.
Pinsker, Z. G. (1978). *Dynamical Scattering of X-rays in Crystals.* Berlin: Springer-Verlag.
Schülli, T. U., Stangl, J., Zhong, Z., Lechner, R. T., Sztucki, M., Metzger, T. H. & Bauer, G. (2003). *Phys. Rev. Lett.* **90**, 066105-1–066105-4.
Shen, Q. (1993). *Acta Cryst.* A**49**, 605–613.
Shen, Q. & Huang, X.-R. (2001). *Phys. Rev. B*, **63**, 174102-1–174102-8.
Snyder, R. L., Fiala, J. & Bunge, H. J. (1999). *Defect and Microstructure Analysis by Diffraction.* Oxford Science Publications.
Stetsko, Y. P., Juretschke, H. J., Huang, Y.-S., Lee, Y.-R., Lin, T.-C. & Chang, S.-L. (2001). *Acta Cryst.* A**57**, 359–367.
Stetsko, Y. P., Lee, Y.-R., Tang, M.-T. & Chang, S.-L. (2004). *Acta Cryst.* A**60**, 64–74.
Stetsko, Y. P., Lin, G.-Y., Huang, Y.-S., Chao, C.-H. & Chang, S.-L. (2001). *Phys. Rev. Lett.* **86**, 2026–2029.
Tanaka, K. & Saito, Y. (1975). *Acta Cryst.* A**31**, 841–845.
Thorkildsen, G. (1987). *Acta Cryst.* A**43**, 361–369.
Thorkildsen, G. & Larsen, H. B. (1998). *Acta Cryst.* A**54**, 120–128.
Thorkildsen, G., Larsen, H. B., Semmingsen, D. & Bjaanes, Ø. (2001). *Acta Cryst.* A**57**, 201–211.
Thorkildsen, G., Larsen, H. B. & Weckert, E. (2001). *Acta Cryst.* A**57**, 389–394.
Thorkildsen, G., Larsen, H. B., Weckert, E. & Semmingsen, D. (2003). *J. Appl. Cryst.* **36**, 1324–1333.
Weckert, E. & Hümmer, K. (1997). *Acta Cryst.* A**53**, 108–143.
Weckert, E. & Hümmer, K. (1998). *Cryst. Res. Technol.* **33**, 653–678.
Wolfram, S. (2003). *The Mathematica Book*, 5th ed. Champain, IL: Wolfram Media.